

Numerical analysis of the influence of magnetic field waveforms on the performance of active magnetic regenerators

Fábio P. Fortkamp · Gusttav B. Lang · Jaime A.

Lozano · Jader R. Barbosa Jr.

Abstract Magnetic cooling is an alternative to vapor compression that does not rely on the use of hazardous substances. The refrigerant is a solid material which reacts to oscillations in magnetic field by changing its temperature (the magnetocaloric effect). In active magnetic regenerators, the magnetocaloric material arranged as a porous medium is subjected to an oscillating fluid flow to allow heat transfer from a cold source to a hot sink in a thermodynamic cooling cycle. Although the literature is abundant with studies on the influence of the fluid flow waveform on magnetic refrigeration devices, the influence of the magnetic field waveform has been much less investigated. In this work, we make use of an active magnetic regenerator numerical model with different mathematically-defined waveforms to determine which operating parameters yield the highest values of cooling capacity and coefficient of

An abridged version of this manuscript was presented at the 24th ABCM International Congress of Mechanical Engineering (COBEM 2017), held in Curitiba, PR, Brazil, in December 2017.

Fábio P. Fortkamp

E-mail: fabio@polo.ufsc.br

Gusttav B. Lang · Jaime A. Lozano · Jader R. Barbosa Jr.

POLO — Research Laboratories for Emerging Technologies in Cooling and Thermophysics, Department of Mechanical Engineering, Federal University of Santa Catarina, Florianópolis, SC, 88040-900, Brazil

performance for a specific set of operating conditions. The results show that the best performance is achieved when the magnetic field is kept constant for the same time duration of the fluid flow through the magnetized material, and that the transition times between the high and low levels of the magnetic field should be as short as possible.

Keywords magnetic refrigeration · active magnetic regenerator · numerical modeling · magnetocaloric effect

List of symbols

Variables

A_{sf}	contact surface area between solid and fluid phases in the regenerator [m^2]
A_t	amplitude of the pressure gradient waveform in the fluid momentum equation [m/s^2]
B	magnetic flux density [T]
c	specific heat [$J/(kg\ K)$]
c_E	Ergun constant of the porous medium
COP	coefficient of performance
D_{ld}	dispersion term in the AMR model [m/s^2]
D_p	particle diameter [m]
f	cycle frequency [Hz]
F_B	blow fraction
F_M	magnetization fraction
$g(t)$	dimensional waveform of the pressure gradient term in the fluid momentum equation
h	heat transfer coefficient [$W/(m^2\ K)$]
H	magnetic field [H]

h	thickness [m]
H_{reg}	regenerator height [m]
K	permeability of the porous medium [m ²]
k	thermal conductivity [W/(m K)]
L_{reg}	regenerator length [m]
\dot{m}_f	mass flow rate [kg/s]
M	magnetization field [H]
m	mass [kg]
N_D	demagnetization tensor
N_{reg}	number of regenerators
N_{valve}	number of valves
ΔP	total pressure drop across one regenerator [Pa]
P	pressure [Pa]
\dot{Q}_C	cooling capacity [W]
\dot{q}_{csg}	volumetric casing losses in the AMR model [W/m ³]
ΔT_{ad}	adiabatic temperature variation [K]
T	temperature [K]
t	time [s]
V	velocity [m/s]
$\dot{W}_{\text{relay},n}$	nominal power consumption of one relay [W]
\dot{W}_{valve}	valve power [W]
$\dot{W}_{\text{valve},n}$	nominal power consumption of one valve [W]
W_{reg}	regenerator width [m]
\dot{W}_{mag}	magnetic power [W]
\dot{W}_{pump}	pumping power [W]

x, y, z coordinate system variables [m]

Greek symbols

β surface area density [m^2/m^3]

ε porosity

Φ utilization factor

$\tan \theta_R$ ramp rate in the magnetic ramp profile [T/s]

ρ density [kg/m^3]

τ time period [s]

$\tau_{0,CC}, \tau_{0,HC}$ time periods without fluid flow in the respective half-cycle (see list of Abbreviations) [s]

τ_B blow duration [s]

τ_M magnetization period in the magnetic ramp profile [s]

τ_R ramp period in the magnetic ramp profile [s]

μ_f fluid dynamic viscosity [Pa s]

μ_0 magnetic permeability of free space [H/m]

Subscripts and Superscripts

air air layer between magnets and regenerators

csg regenerator casing

eff effective

f fluid phase

p constant-pressure

s solid phase

sf relative to the heat transfer between solid and fluid phases in the regenerator

x yttrium fraction

Abbreviations

C	cold source
CB	cold blow
CC	cold cycle
CE	cold end
H	hot source
HB	hot blow
HC	hot cycle
IT	instantaneous magnetic profile
AMR	Active Magnetic Regenerator
MCE	Magnetocaloric Effect
MCM	Magnetocaloric Material
MR	Magnetic (or Magnetocaloric) Refrigeration
RC	rectified cosine magnetic profile
RM	ramp magnetic profile

1 Introduction

Although mechanical vapor compression has been the dominant cooling technology for the past century [1], it still faces a number of challenges related to its environmental footprint. For instance, the phase-out of refrigerants with ozone depleting and global warming potentials brought about a more widespread use of flammable substances, which pose a new set of concerns, restrictions and new technological challenges for consumer applications [2, 3].

Magnetic refrigeration (MR) is an emerging cooling technology which does not rely on hazardous fluids. In MR, the temperature of a *magnetocaloric material* (MCM) changes as a result of cyclical changes in the applied magnetic field due to the so-called *magnetocaloric*

effect (MCE). The magnitude of the MCE depends on material properties, magnetic field variation and temperature, and it is maximum at the Curie temperature of the material [4, 5]. Applications of the MCE at near room-temperature are not restricted to cooling applications [6, 7]; it can also be applied to the development of thermomagnetic motors [8].

For operating temperatures typical of household cooling applications, the MCE is of the order of 2-5 K/T. To amplify this temperature change, heat regeneration is usually employed [5]. Active magnetic regenerators (AMR) are thermal devices in which the magnetocaloric material is packed as a porous matrix subjected to periodic flow of an aqueous heat transfer fluid. The flow is put in sync with successive magnetization and demagnetization steps of the MCM in the porous bed to produce a refrigerating effect. Thus, the AMR is essentially a cascade of infinitesimal “layers” of MCM that are activated simultaneously to build up a longitudinal temperature profile in the matrix. The layers can be made of the same material, resulting in a homogeneous regenerator. However, given the dependence of the MCE on temperature, it is desirable to build *multilayer* regenerators, where each adjacent layer has a slightly different composition that will function around its own Curie temperature, maximizing the magnetocaloric effect of each portion.

A typical AMR cycle is comprised of the following steps: (i) The magnetic circuit magnetizes the MCM, thereby increasing its temperature due to the MCE; (ii) During the *cold blow*, cold fluid previously in thermal contact with the low-temperature source flows through the warm bed, absorbs its energy and releases it as heat to the high-temperature sink through the hot heat exchanger; (iii) The MCM is demagnetized and cooled down as a result; (iv) As the fluid flow is reversed (*hot blow*), it releases energy to the bed, and decreases its temperature so it can absorb the thermal load at the cold heat exchanger in contact with the low-temperature source. Different cycles can be devised by changing the duration and synchronization between the two cycle *characteristic waveforms*:

1. The *applied magnetic field profile*, which describes the oscillating magnetic field over one regenerator;
2. The *fluid flow profile*, which describes the time-variation of flow rate through one bed.

Fluid flow profiles can be more easily investigated experimentally, as no changes in the fluid flow hardware are required, provided a reliable and flexible valving system is in place. In particular, the effect of the *duration* of the fluid blows has been extensively investigated [9, 10, 11]. There appears to be a consensus in the literature that the cooling capacity of magnetic refrigerators can be increased by displacing the fluid during periods where the magnetic field is at its extreme values.

The control of these blow durations can be achieved with the use of solenoid valves; a model for a digital hydraulic system and a calculation of valve power has been presented by [12] and [13]. An application of electronic valves in AMR devices has been presented by [14], using the control logic (for synchronizing the valve operation with the magnetic profile) described by [15].

In contrast, because of the complexities involved in designing and fabricating magnetic circuits, the applied magnetic field profiles (or simply the magnetic waveforms) are much less studied, and are usually investigated in terms of their synchronization with the fluid flow profile with numerical investigations. Considering a trapezoidal magnetic profile and a square fluid flow waveform, a numerical analysis showed that small delays between the increase of the magnetic field and the start of the fluid flow is beneficial for the cooling capacity, to assure the solid is fully magnetized before the fluid starts transferring energy from it [16]. To the authors' knowledge, the only work that experimentally varied the magnetic profile, by controlling the rotation of magnetic cylinders, is the work by [17], which also

showed that cooling capacity of an AMR device is dependent on this lag between magnetization and fluid flow.

If this delay is further increased so that the fluid flow period can coincide with different stages of the magnetic profile, different thermodynamic cycles can be obtained with different performance trends; the Brayton AMR cycle (explained previously) yields the highest cooling capacities, while the Ericsson AMR cycle (with isothermal (de)magnetization steps) yield the highest values of the coefficient of performance [18]. This conclusion was confirmed by the more extensive numerical analysis of [5], which also varied the amplitude of the trapezoidal magnetic profile and proposed magnetic circuit designs which could generate these profiles. Trevizoli et al. [19] carried out a numerical comparison of the square wave (step change), sinusoidal and rectified cosine magnetic profiles for a sinusoidal fluid profile and concluded that the cooling capacity and maximum temperature spans are maximal for the instantaneous magnetic profile.

As previously noted, the fluid flow profile is implemented with proper design of the fluid flow system, while the magnetic profile is an important input when designing a magnetic circuit [20]. With the goal of AMR design, none of works reviewed in this section considered different *shapes* and *amplitudes* of the magnetic field waveform. Regarding shape, the combination of a trapezoidal magnetic profile and an instantaneous fluid flow profile is prevalent in the literature [16, 17, 21], and this case is also investigated in the present paper. However, sinusoidal magnetic profiles can be achieved with more compact systems [22], and their generation and impact of AMR devices have been investigated by our group [23, 24], but no work has investigated how these waveforms, when synchronized with optimized fluid flow profiles, can compare with the instantaneous magnetic profile, which the literature identifies as the optimal one when the fluid flow profile is fixed.

The present work bridges the gaps left in previous studies by investigating the performance of a magnetic refrigerator under different magnetic profile waveforms. These waveforms are mathematically modeled, and the cooling capacity and coefficient of performance are calculated based on the profiles parameters, while also investigated how the AMR geometry affect the performance in combinations with the magnetic profile. The fluid flow profile is assumed fixed in shape, although its parameters are also varied. To emulate constraints on an operating point of actual magnetic refrigeration devices, the temperature span is set fixed, and hence few comments are made on second-law efficiency.

2 Materials and methods

As previously explained, we performed numerical simulations using a previously developed AMR model, varying the profile-specific and geometric parameters. We also implemented a model to calculate the power consumption of a novel fluid management system, which is a topic not yet extensively studied in the literature. The output variables from this integrated model are the cooling capacity, the several power contributions (the magnetic power to magnetize the material, the pumping power to overcome pressure drop in the regenerator, and the power to actuate the electronic valves) and the coefficient of performance (COP).

2.1 AMR model

2.1.1 Governing equations

Simulations were performed using a one-dimensional AMR mathematical model, implemented using the Finite Volume Method [25]. The model solves momentum and energy balance equations for the solid and fluid phases, represented by indices ‘s’ and ‘f’, respectively.

The model geometry is shown in Figure 1, and assumes that the regenerator is composed of monodisperse packed spheres with porosity ε .

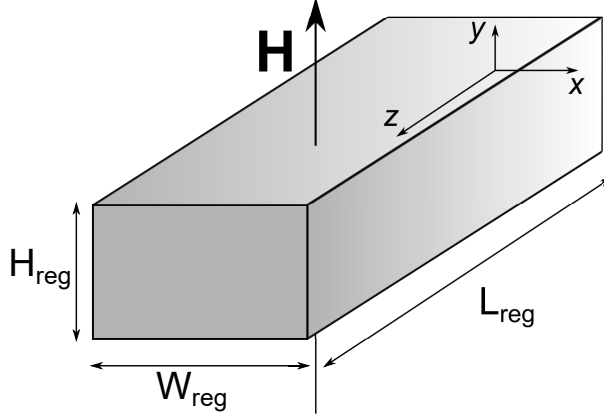


Fig. 1: AMR model geometry

The momentum equation for the fluid domain is given by:

$$\frac{\rho_f}{\varepsilon} \frac{\partial V_z}{\partial t} = -\frac{\partial P}{\partial z} - \frac{\mu_f}{K} V_z - \frac{c_E \rho_f}{K^{1/2}} |V_z| V_z \quad (1)$$

where the macroscopic inertial term on the left-hand side is balanced with the pressure gradient, Darcy stress and Forchheimer drag [26]. The momentum equation is solved for the time-dependent uniform fluid velocity V_z through the bed.

The energy equation for the fluid phase can be written as:

$$\begin{aligned} \rho_f c_{p,f} \left(\varepsilon \frac{\partial T_f}{\partial t} + V_z \frac{\partial T_f}{\partial z} \right) = & -\dot{h}_{sf} \beta (T_f - T_s) \\ & + \left| V_z \frac{\partial P}{\partial z} \right|_f \\ & + \varepsilon \left(k_f^{\text{eff}} + \rho_f c_{p,f} D_{ld} \right) \frac{\partial^2 T_f}{\partial z^2} \\ & + \dot{q}_{csg} \end{aligned} \quad (2)$$

where the left-hand side includes the inertial and advection terms, and the right-hand side includes terms for the solid-fluid heat transfer, viscous dissipation, heat conduction, porous-media dispersion, and casing losses.

The energy equation for the solid phase is written as:

$$\rho_s c_s (1 - \varepsilon) \frac{\partial T_s}{\partial t} = \hbar_{sf} \beta (T_f - T_s) + (1 - \varepsilon) k_s^{\text{eff}} \frac{\partial^2 T_s}{\partial z^2} \quad (3)$$

where the terms represent respectively inertia, solid-fluid heat transfer and heat conduction.

Initial and boundary conditions, closure relations for the porous media terms, solution methods and convergence criteria and analyses are discussed in detail in [25]. This AMR model solves the above equations for one regenerator operating between given sources temperatures (assuming ideal heat exchangers in contact with the thermal reservoirs), during one full cycle (hot and cold blows and magnetization and demagnetization periods), given specified operating conditions (to be discussed later).

The casing heat transfer term \dot{q}_{csg} in Equation 2 is calculated solving the heat conduction equation in the regenerator casing [25]. It can be neglected in some circumstances if an insulating casing material is assumed, which greatly simplifies the analysis.

2.1.2 Fluid flow profile modeling

The pressure gradient in Equation 1 is modeled as:

$$-\frac{\partial P}{\partial z} = \rho_f A_t g(t) \quad (4)$$

where $g(t)$ is a dimensionless function that expresses the mathematical waveform of the pressure gradient, and A_t is its amplitude, adjusted in a convergence loop. In this loop, the

mass flow rate calculated in term of the Darcy velocity from Equation 1 is compared with the input mass flow rate until convergence is obtained.

The canonical fluid flow profile considered in this work is the square wave or *instantaneous profile*, because of the instantaneous change in flow rate, as shown in Figure 2.

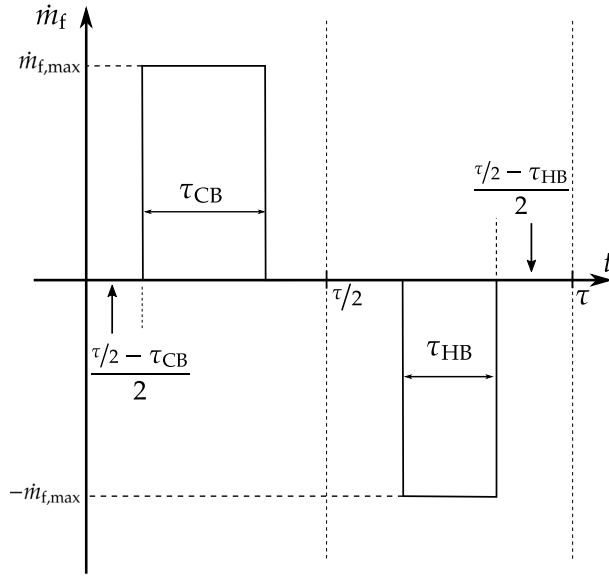


Fig. 2: Instantaneous fluid flow profile. Adapated from [24].

The instantaneous mass flow rate, $\dot{m}_f(t)$, is defined over a cycle with a period τ , and represents the fluid flow through a given regenerator bed. The so-called *hot cycle*, during which the MCM is magnetized, occupies the time interval $0 \leq t < \tau/2$, while the *cold cycle* lies between $\tau/2 \leq t \leq \tau$. The flow profile oscillates between two plateaus of equal magnitude $\dot{m}_{f,max}$ and opposite directions, which are centered in each half-cycle. During the hot cycle, the cold blow period is τ_{CB} , and during the cold cycle the hot blow period is τ_{HB} . If balanced flow exists, then $\tau_{CB} = \tau_{HB}$.

During each half cycle, there are periods without fluid flow defined as:

$$\tau_{0,HC} = \frac{\tau/2 - \tau_{CB}}{2} \quad (5)$$

$$\tau_{0,CC} = \frac{\tau/2 - \tau_{HB}}{2} \quad (6)$$

where HC and CC stand for hot cycle and cold cycle, respectively.

The profile can be mathematically defined as:

$$\dot{m}_f(t) = \begin{cases} 0, & 0 \leq t < \tau_{0,HC} \\ \dot{m}_{f,max}, & \tau_{0,HC} \leq t \leq \tau/2 - \tau_{0,HC} \\ 0, & \tau/2 - \tau_{0,HC} < t < \tau/2 + \tau_{0,CC} \\ -\dot{m}_{f,max}, & \tau/2 + \tau_{0,CC} \leq t \leq \tau - \tau_{0,CC} \\ 0, & \tau - \tau_{0,CC} < t < \tau \end{cases} \quad (7)$$

When the blows have different time durations, the AMR cycle is considered unbalanced, and that is known to have a negative effect on performance [27, 10]. In this work, the blows are always balanced, hence the blow fraction, i.e., the ratio of blow durations to cycle period [10], can be evaluated as:

$$F_B = \frac{2\tau_B}{\tau} \quad (8)$$

where τ_B is the duration of one blow.

2.1.3 Magnetic profile modeling

The magnetic profile is modeled by a waveform of magnetic field strength, $H(t)$, applied perpendicular to the regenerators, as shown in Figure 1. The magnetic field is assumed

uniform throughout the beds. The applied field is corrected from demagnetization effects to yield the effective field inside the regenerators:

$$H^{\text{eff}} = H - N_D M \quad (9)$$

where M is the magnetization field of the material, and N_D is a demagnetization factor.

The magnetocaloric effect is implemented in the so-called discrete approach [28]; every time the magnetic field changes, based on the input magnetic profile, the solid temperature is calculated according to:

$$T_s(t + \Delta t) = T_s(t) + \Delta T_{\text{ad}} \left(T_s(t), H^{\text{eff}}(t), H^{\text{eff}}(t + \Delta t) \right) \quad (10)$$

where the adiabatic temperature variation, ΔT_{ad} , a standard measure of the MCE, is calculated from tabulated experimental data for magnetocaloric materials as function of temperature and effective field. [25]. Experimental curves of ΔT_{ad} can be found in [29].

The magnetic profiles considered in this work are presented in terms of the flux density $B = \mu_0 H$, where μ_0 is the permeability of free space; the magnetic field H is used in the evaluation of the magnetocaloric effect (cf. Sec. 2.1.3).

The instantaneous (square wave) profile (represented by the subscript “IT”) and the rectified cosine profile (represented by “RC”) are defined solely in terms of the extreme values B_{min} and B_{max} , and are shown in Figure 3.

$$B_{\text{IT}}(t) = \begin{cases} B_{\text{max}}, & 0 \leq t < \tau/2 \\ B_{\text{min}}, & \tau/2 \leq t < \tau \end{cases} \quad (11)$$

$$B_{\text{RC}}(t) = B_{\text{min}} + (B_{\text{max}} - B_{\text{min}}) \left| \cos \left(\frac{\pi}{\tau} \left(t - \frac{\tau}{4} \right) \right) \right| \quad (12)$$

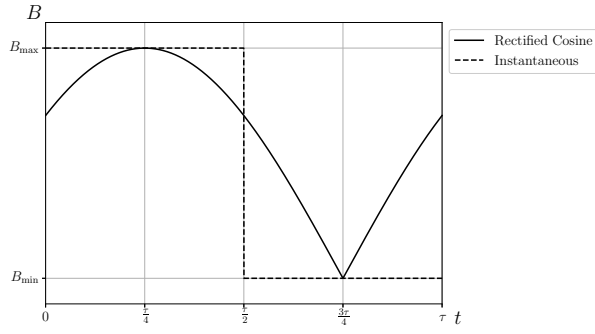


Fig. 3: Instantaneous ("IT") and rectified cosine ("RC") magnetic profiles

A suitable approximation of the instantaneous profile is the *magnetic ramp profile*, shown in Figure 4, with finite transition times between the levels of constant magnetization. The magnetic profile oscillates between a low value B_{\min} and a high value B_{\max} , and remains at each plateau for a period of τ_M . The plateaus are balanced and centered at each half-cycle.

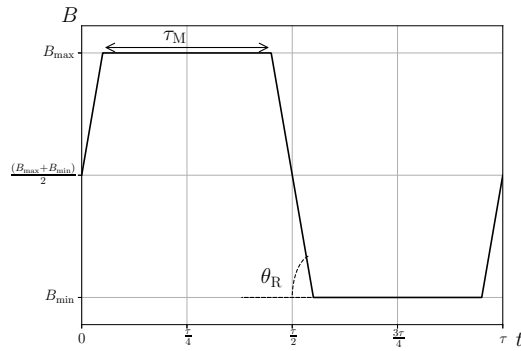


Fig. 4: Magnetic ramp profile

The *ramp period* τ_R is defined as:

$$\tau_R = \frac{1}{4} (\tau - 2\tau_M) \quad (13)$$

such that there are four ramp periods in one full cycle. The ramp rate, $\tan \theta_R$, is:

$$\tan \theta_R = \frac{(B_{\max} - B_{\min})}{2\tau_R} \quad (14)$$

The magnetization fraction, F_M , is the fraction of the cycle during which the magnetocaloric material is subjected to a constant magnetic field:

$$F_M = \frac{2\tau_M}{\tau} \quad (15)$$

The ramp profile (“RM”) can be mathematically defined as:

$$B_{RM}(t) = \begin{cases} (B_{\max} + B_{\min})/2 + t \tan \theta_R, & 0 \leq t < \tau_R \\ B_{\max}, & \tau_R \leq t < \tau/2 - \tau_R \\ B_{\max} - (t - (\tau/2 - \tau_R)) \tan \theta_R, & \tau/2 - \tau_R \leq t < \tau/2 + \tau_R \\ B_{\min}, & \tau/2 + \tau_R \leq t < \tau - \tau_R \\ B_{\min} + (t - (\tau - \tau_R)) \tan \theta_R, & \tau - \tau_R \leq t \leq \tau \end{cases} \quad (16)$$

Additionally, the average values of the magnetic field during each half-AMR cycle are considered for comparison between profiles. The average magnetic profile during the hot cycle ($0 \leq t < \tau/2$) is denoted by \bar{B}_{high} and the average during the cold cycle ($\tau/2 \leq t < \tau$) is denoted by \bar{B}_{low} . For the instantaneous waveform, these average values are identical to the extreme values.

2.1.4 Evaluation of solid and fluid properties

The fluid properties are considered constant in the momentum equation to decouple the solution procedures to determine the velocity and temperature fields. The properties are computed at the average temperature between the hot and cold sources, and are evaluated

from interpolation of tables imported from the EES software [30]. In all simulations shown in this work, the heat transfer fluid is a 80/20 % vol. mixture of water/ethylene-glycol. For the energy equations, the fluid properties are also calculated from tabulated data, but the temperature dependence is considered.

Both single- and multilayer regenerators are considered in this study. Single-layer regenerators are composed of gadolinium, a benchmark material with a Curie temperature of 290 K. For simplicity, the solid density is assumed constant at $\rho_s = 7900 \text{ kg/m}^3$ and the solid thermal conductivity is set to $k_s = 10.5 \text{ W/(mK)}$. The specific heat capacity of Gd is calculated as a function of temperature and magnetic field based on experimental data, using a bi-linear interpolation scheme; more details on the experimental dataset are available in [25].

For the multilayer simulations, alloys of gadolinium and yttrium are used in the form $\text{Gd}_{1-x}\text{Y}_x$, where x is the yttrium fraction. This fraction reduces the Curie temperature of the alloy relative to that of pure gadolinium. Due to the lack of experimental data on the magnetocaloric properties of $\text{Gd}_{1-x}\text{Y}_x$ alloys at the time this analysis was made, a simpler approach was used in which the dependence of magnetization, specific heat capacity and entropy with respect to the magnetic field for alloys with a low yttrium fraction are identical to those of pure gadolinium, but are shifted to a lower Curie temperature (corresponding to the yttrium fraction).

2.1.5 Performance metrics

The AMR model is solved for only one bed, but assumes that the N_{reg} identical beds experience the same cycle. Thus, the extensive performance parameters are multiplied by that factor.

The cooling capacity is calculated as [25]:

$$\dot{Q}_C = N_{\text{reg}} \frac{1}{\tau} \int_{\tau_{\text{HB}}} \dot{m}_f(t) c_{p,f} (T_C - T_{f,\text{CE}}) dt \quad (17)$$

As pointed out in [24], since external sources of irreversibility (e.g., heat transfer with a finite temperature difference in the heat exchangers) are ignored and no eddy currents and hysteresis losses are present, the magnetic power required to magnetize the solid refrigerant and produce the MCE in the AMR cycle is given by the product of the Carnot efficiency and the cooling capacity as follows:

$$\dot{W}_{\text{mag}} = \dot{Q}_C \frac{T_H - T_C}{T_C} \quad (18)$$

Irreversibility due to fluid friction is accounted for in the calculation of the pumping power:

$$\dot{W}_{\text{pump}} = N_{\text{reg}} \frac{1}{\tau} \int_0^\tau \frac{\dot{m}_f}{\rho_f} \Delta P dt \quad (19)$$

where ΔP is the total pressure drop through the regenerator (including one hot and one cold blow).

2.2 Hydraulic system and fluid flow profile model

The hydraulic system designed to modulate the fluid flow through different regenerators at different time instants is composed of a pump and a set of electronic valves which can be precisely controlled to yield the desired blow durations. The electrical power consumed by the valve array is computed separately from other work contributions.

In the present analysis, two types of valves are considered. In the first approach, called *Type R valves*, the model proposed in [12] is used, assuming that the individual consumption

of each valve is independent of frequency and blow fraction. The valve power \dot{W}_{valve} can be computed as:

$$\dot{W}_{\text{valve}} = N_{\text{v}} F_{\text{B}} \left(\dot{W}_{\text{valve},n} + \frac{1}{2} \dot{W}_{\text{relay},n} \right) \quad (20)$$

where N_{valve} is the number of valves, $\dot{W}_{\text{valve},n}$ is the measured average nominal power for one normally-closed electronic valve and $\dot{W}_{\text{relay},n}$ is the nominal power for one controlling relay. The factor $1/2$ is due to two valves being controlled by one relay.

In the second approach, *Type S* valves are used, with nominal power lower in magnitude but which depends on frequency and blow fraction. These valves were experimentally characterized by [13], where a single valve was attached to a measurement circuit and set to operate for varying values of blow fraction and frequency; the valve power was calculated from the averaged values of voltage and current after periodic steady state was reached. From these experiments, the valve power was experimentally correlated as:

$$\dot{W}_{\text{valve}} [\text{W}] = N_{\text{valve}} (0.927f [\text{Hz}] + 1.023F_{\text{B}} + 0.226f [\text{Hz}]F_{\text{B}} - 0.037) \quad (21)$$

Equation (21) was correlated for blow fractions of 50 and 100 % and frequencies in the range of 0.2–1.6 Hz, with an uncertainty on the order of 0.4 W for a single valve. The use of different valve types will be discussed among the presented results.

Independent of the valve type used, it is also assumed that each valve system can produce the fluid flow profile shown in Figure 2, where the displaced fluid mass during one blow in one regenerator bed is $\dot{m}_{\text{f,max}} F_{\text{B}} \tau / 2$. The *utilization factor* can then be calculated as:

$$\Phi = \frac{\dot{m}_{\text{f,max}} F_{\text{B}} c_{\text{f}}}{2f m_{\text{s}} c_{\text{s}}} \quad (22)$$

and in all results shown in this work, the number of valves is calculated as:

$$N_{\text{valve}} = 2N_{\text{reg}} \quad (23)$$

2.3 Calculation of the coefficient of performance

The coefficient of performance takes the cooling capacity as the main output parameter from the AMR model, in addition to all previously cited power contributions:

$$\text{COP} = \frac{\dot{Q}_c}{\dot{W}_{\text{pump}} + \dot{W}_{\text{mag}} + \dot{W}_{\text{valve}}} \quad (24)$$

3 Results and Discussions

The analysis of magnetic profiles was performed at two different stages. Initially, the instantaneous (square-wave) and the rectified cosine profiles are compared using a simpler approach (i.e., neglecting casing losses). Later, based on the selection of the most promising magnetic profile, a more in-depth analysis is carried out to determine the optimal geometric and operating parameters of the AMR system.

3.1 Comparison of instantaneous and rectified cosine profiles using a simplified model

At the first stage of the present analysis, the instantaneous and rectified cosine profiles are compared considering a single-layer regenerator without casing losses, using Type R valves. The parameters used in all simulations are presented in Table 1.

When comparing the performances resulting from the application of the different magnetic profiles, the same average magnetic field during the hot cycle will be considered; this implies a higher peak for the rectified cosine. For the cold cycle, the minimum values for

Table 1: AMR parameters kept fixed in the simulations with different magnetic profiles

Parameter	Value
D_p	0.5 mm
H_{reg}	20 mm
W_{reg}	25 mm
L_{reg}	100 mm
N_{reg}	11
N_{valve}	22
T_H	298 K
T_C	278 K
$\dot{W}_{\text{valve},n}$	4 W
$\dot{W}_{\text{relay},n}$	0.36 W

both profiles are the same, as shown in Figure 5. For reference, in all simulations, the minimum value for the rectified cosine was fixed at $B_{\text{min}} = 0.1$ T.

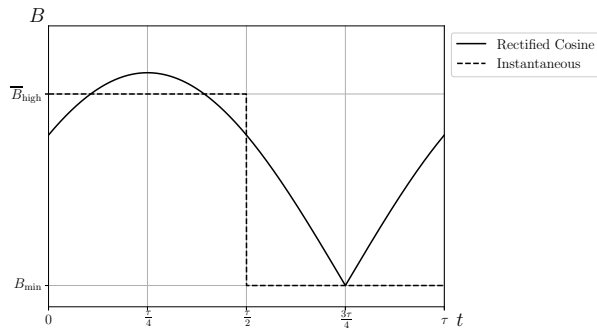


Fig. 5: Configuration of average and extreme values of the instantaneous and rectified cosine profiles

Simulations were carried out for various values of blow fraction. The rectified cosine profile can benefit from a smaller blow fractions that concentrate the flow during the periods

of very high and very low fields, thereby increasing the average variation in magnetic field [10]; this does not happen with the instantaneous profile, since the field is constant and reducing the blow fraction will only reduce the period where the fluid is in contact with the warmed up solid, decreasing the regenerator effectiveness. In this section, all results use the critical value of blow fraction that maximized the cooling capacity: fluid flowing during the entire period for the instantaneous profile, and only during 60 % of the period (the smallest blow fraction tested) for the cosine profile; this latter case is shown in Figure 6.

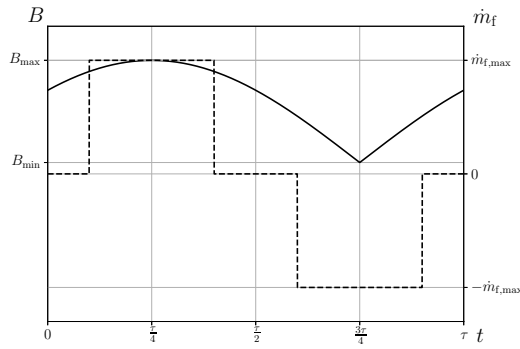


Fig. 6: Rectified cosine magnetic profile and the instantaneous flow profile with blow fraction of 60 %

Figure 7 shows the cooling capacity attained by the device at a frequency of 1 Hz and different utilizations. The horizontal axis shows the average field value during the high field region. The instantaneous profile almost always yields a higher performance, and since the average field during the hot cycle (high field stage) is the same, the main difference is due to the low magnetic field levels. In this comparison, the instantaneous profile is capable of keeping a low magnetic field over the entire half-cycle, which is beneficial for performance; for $\Phi = 1.0$ and $B_{\text{high}} = 1.40 \text{ T}$, the cooling capacity for the instantaneous profile is 196.3% higher than for the cosine profile. As demonstrated by [19], a higher average magnetic field

during the low-field stage increases the solid temperature and consequently results in warmer fluid entering the cold heat exchanger, representing a thermal loss.

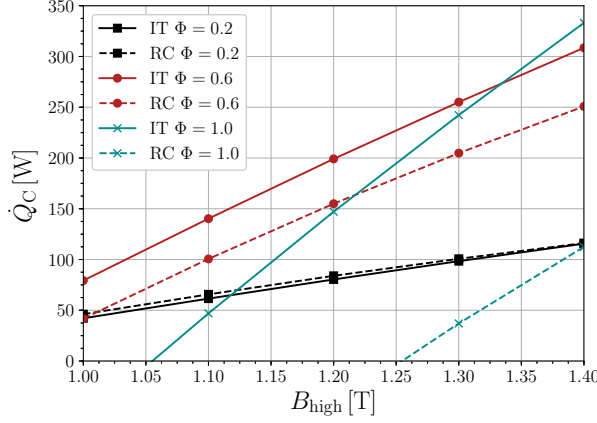


Fig. 7: Cooling capacity as a function of the average high magnetic field, for different utilizations. “IT”: instantaneous (blow fraction of 100 %); “RC”: rectified cosine (blow fraction of 60 %).

The only exception in this comparison is observed for the lowest utilization of $\Phi = 0.2$, where the performance is slightly better for the RC profile. Since the blow fraction for the cosine is smaller, the mass flow rate is higher in the latter for the same utilization (cf. Eq. (12)). This increases the heat transfer rate, as previously explained — outweighing the effects of the magnetic field.

The same analysis, but in terms of the coefficient of performance, is shown in Figure 8, where the instantaneous profile yields better results for medium to high levels of utilization. This is explained by the behavior of the magnetic, valve and pumping power shown in Figure 9 for a fixed utilization of 0.6. As can be seen, the magnetic power only differs between the profiles due to changes in cooling capacity. Also, the valve power is higher for

the instantaneous profile since the valves must remain open for longer periods. However, the proportional increase in pumping power, due to larger flow rates, is even higher (than the change in valve power).

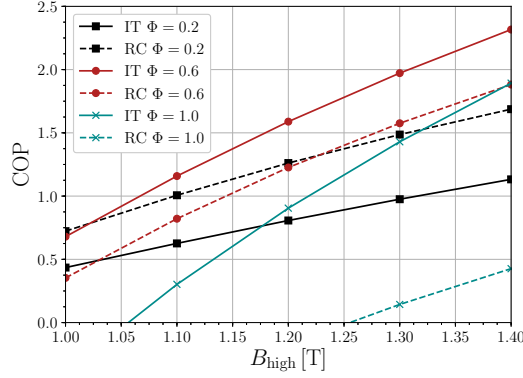


Fig. 8: Coefficient of performance as a function of the average high magnetic field, for different values of utilization. “IT”: instantaneous (blow fraction of 100 %); “RC”: rectified cosine (blow fraction of 60 %).

In general, considering target values for the cooling capacity, AMRs operating with the instantaneous magnetic profile lead to better performance results. As can be seen in Fig. 7, an instantaneous profile with the lowest possible value of B_{min} and the highest possible value of B_{max} , with a flow profile occupying the whole cycle with average values of utilization, results in the highest values of cooling capacity among all simulations.

The rectified cosine profile, found in compact systems using Halbach arrays, can surely benefit from reducing the blow fraction, both in terms of cooling capacity and temperature span. However, for the typical parameters evaluated in this paper, even if the blow fraction is optimized for the “RC” profile, the “IT” profile still gives better results.

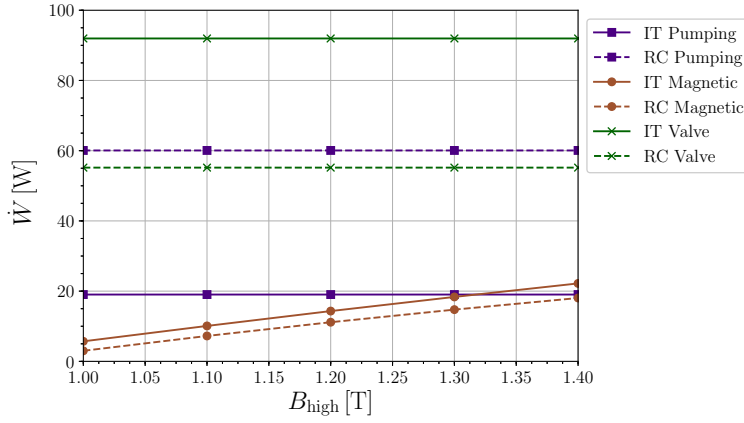
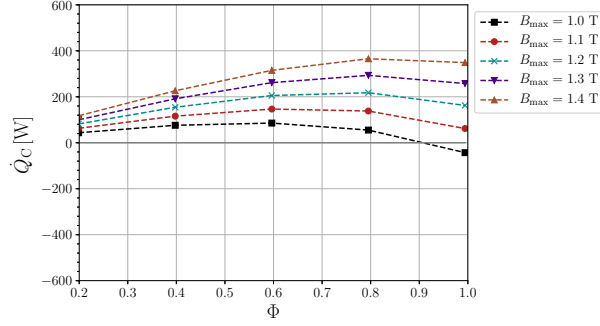


Fig. 9: Power contributions as functions of the average high magnetic field, for a utilization of 0.6. “IT”: instantaneous (blow fraction of 100 %); “RC”: rectified cosine (blow fraction of 60 %).

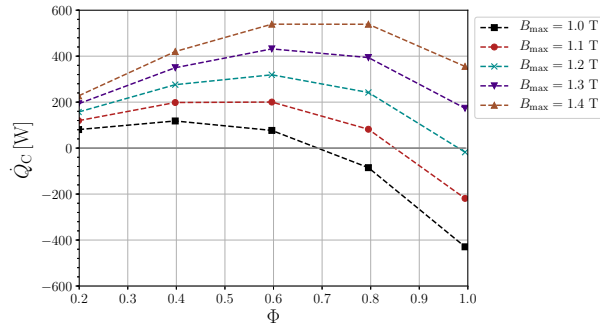
3.1.1 Analysis of the instantaneous profile

As shown in the previous section, the instantaneous profile generally yields the highest values of cooling capacity. Therefore, in this section, a more detailed analysis of this profile is carried out, where the maximum field is varied, but the minimum value is kept at 0.05 T. Figure 10 shows the cooling capacity as a function of the utilization, for several levels of the maximum magnetic field and two different operating frequencies. Because of the conflict between a low heat transfer rate for flow rates that are too low and losses in regenerator effectiveness in flow rates that are too high, there are critical values of utilization that maximize the cooling capacity, and these critical values increase with the magnetic field. For higher magnetic fields, the increase in the MCE surpasses the loss of effectiveness, and one can go to higher flow rates without losing performance. It can also be seen in Fig. 10 that at higher frequencies the values of cooling power are higher, and also the critical values

of utilization are lower. However, this is usually achieved at the expense of a higher power consumption in AMR devices at higher frequencies [31, 32].



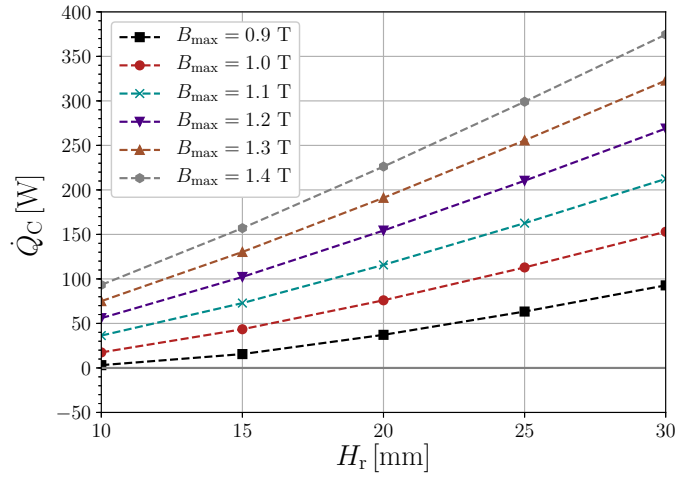
(a) $f = 1 \text{ Hz}$



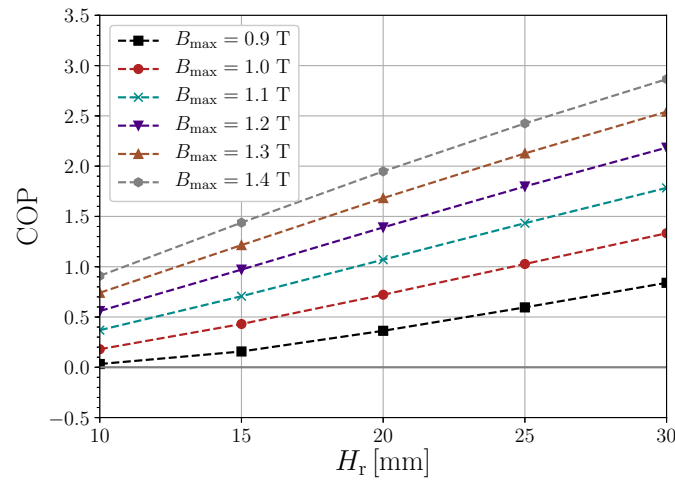
(b) $f = 2 \text{ Hz}$

Fig. 10: Cooling capacity as a function of utilization, for various values of the high magnetic field for the instantaneous profile

The geometric parameters in Table 1 were chosen from preliminary simulations, so they are not optimal. To understand the impact of the regenerator geometry on the system performance with the instantaneous profile, the regenerator height was varied in Fig. 11, and all other parameters from Table 1 were kept fixed and with $\phi = 0.4$. As expected, higher magnetic fields allow for smaller regenerators (hence more compact systems) to achieve a



(a) Cooling capacity



(b) Coefficient of performance

Fig. 11: Performance metrics as a function of the regenerator height (all other parameters were set as in Table 1, for utilization factor of 0.4) for various values of the high magnetic field of the instantaneous profile

desired cooling capacity. For instance, to achieve a capacity of 100 W, increasing the field from 1.0 to 1.2 T results in regenerators that are 36 % smaller. Comparing the results for

the cooling capacity and coefficient of performance, the trends are largely the same, as the former is more sensitive to variations in the magnetic field and regenerator height than the components of power.

3.2 In-depth analysis of the magnetic ramp profile

Based on the better performance of the instantaneous profile, the ramp profile is a naturally suitable target profile for the design of magnetic refrigerators, and will be analyzed in this section, representing the second stage in the analysis of magnetic profiles.

Moving towards a more realistic model, casing losses are included, using the model from [25]. The bed is enclosed in a solid casing of thickness h_{csg} , and two air layers of thickness h_{air} separate the AMR and its casing from the inner and outer magnet cylinders, as shown in Figure 12. The optimal design of such magnetic cylinders aiming at a particular magnetic profile will be the subject of future publications.

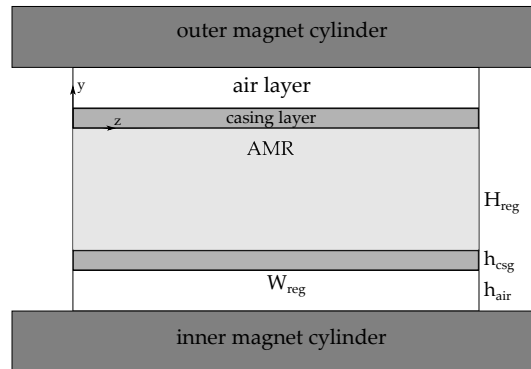


Fig. 12: Model for the casing losses in regenerators

Preliminary analyses carried out by [33] showed that a stainless steel casing with a thickness of $h_{\text{csg}} = 0.5 \text{ mm}$ is thick enough to ensure mechanical integrity and easy manufacturing, while being thin enough to accommodate the material with a low thermal conductivity.

In addition, in the present study, an air gap clearance thickness was set at $h_{\text{air}} = 1 \text{ mm}$. This value gave rise to a peak in cooling capacity due to the compromise between minimizing losses and maximizing the magnetocaloric mass. The thermophysical properties of stainless steel and air were also obtained with interpolation of tables exported by the EES software [30].

The simulations in this section also use multilayer regenerators. A summary of all parameters adopted in this section, including the Curie temperatures and volumetric fractions (relative to the length of the bed) of each layer is presented in Table 2. In addition, in the following results, Type S valves are used, with valve power calculated by Equation 21.

Figure 13 shows the two profiles that will be used in this section and how they are synchronized. Regarding the magnetic profile, the magnitude of the high value will be varied to investigate the performance of the AMR system, while the minimum will be kept at $B_{\text{min}} = 0.05 \text{ T}$.

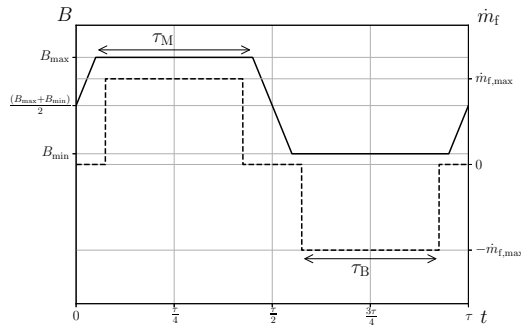


Fig. 13: Comparison between the magnetic ramp profile (solid line) and the instantaneous fluid flow profile (dashed line)

Parameter	Value
W_{reg}	30 mm
L_{reg}	85 mm
N_{reg}	8
N_{valve}	16
f	1 Hz
T_{H}	305.5 K = 32.5 °C
T_{C}	270.5 K = -2.5 °C
D_{p}	350 μm
h_{csg}	0.5 mm
h_{air}	1 mm
Casing material	Stainless steel
Number of layers	3
Curie temperatures of each layer	273, 283, 290 K
Length fractions of each layer	20, 20, 60 %

Table 2: Fixed parameters for the AMR simulations used in this chapter

3.2.1 Performance curves for variable blow and magnetization fractions

Figure 14 shows the cooling capacity and coefficient of performance of the AMR system for a fixed utilization factor of 0.4 and for a magnetic profile with a maximum at 1.3 T, for variable blow and magnetization fractions. To facilitate the analysis, the results are plotted in terms of the ratio $F_{\text{M}}/F_{\text{B}}$, with curves for different values of F_{B} . It is clear that both the cooling capacity and the coefficient of performance exhibit a peak at $F_{\text{M}} = F_{\text{B}}$. Moreover, to the right of the peak, i.e., for higher values of F_{M} , the reduction of both performance metrics is slower, meaning it is better to have a magnetization plateau that is wider than the fluid flow plateau.

The reduction in performance for $F_M > F_B$ can be explained by an increase in heat leakage through the casing, as the solid begins to lose energy to the environment when the fluid is not flowing. For $F_M < F_B$, the fluid begins to flow when the solid is not totally warmed up, losing effectiveness.

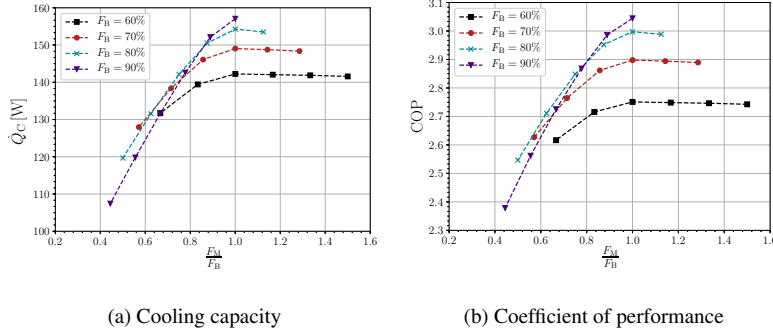


Fig. 14: Performance of the AMR system for various blow and magnetization fractions, utilization of 0.4 and and high magnetic field of 1.3 T

The influence of the utilization is demonstrated in Figure 15, where the cooling capacity is plotted for different utilization factors. For increasing Φ in this range, not only do the overall values of cooling capacity increase, but also the importance of choosing the blow fraction becomes clearer. In these ranges of utilization and blow fraction, the cooling capacity increases because the higher transfer rate associated with higher flow rates dominates over the loss of regenerator effectiveness.

The above results can be evaluated from another point of view with Figure 16, where the coefficient of performance is plotted as contour levels. This type of map is useful because, since B_{\min} and τ are fixed, each point in this graph completely characterizes a magnetic ramp profile, and each subplot with fixed Φ and F_B characterizes the fluid flow profile.

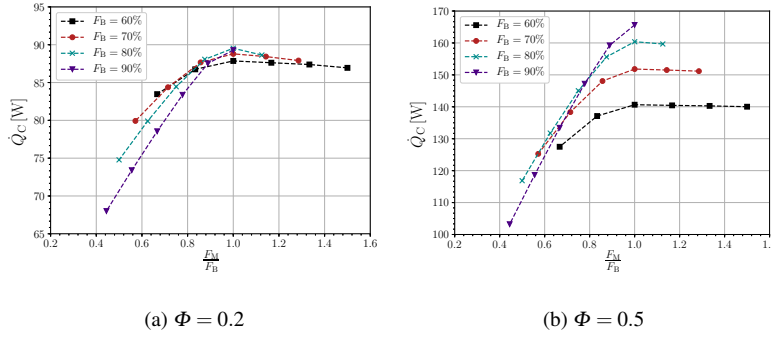


Fig. 15: Influence of utilization on the cooling capacity of the AMR system for various blow and magnetization fractions, with high magnetic field of 1.3 T

As expected, the performance increases for the higher values both B_{\max} and F_M , where the magnetic ramp profile tends to the instantaneous magnetic profile with a large amplitude. Confirming the previous trends, the results are less sensitive to the magnetization fraction when $F_M \geq F_B$.

3.2.2 Geometric analysis of the regenerators using the magnetic ramp profile

All previous results assumed a fixed regenerator geometry, with the goal of identifying the optimal fluid and magnetic profile parameters. It became clear that the magnetization fraction should be as large as possible, but that raises some challenges in realizing abrupt changes in the magnetic field. The value of $F_M = 70\%$ is then chosen as a compromise, with a corresponding $F_B = F_M$. The mean value of the utilization factor of $\Phi = 0.4$ is also chosen as reference in the next results.

Figure 17 shows the cooling capacity, coefficient of performance and second-law efficiency for varying magnetic field and regenerator height. As expected, larger regenerators can produce the desired performance with lower magnetic fields. It can also be seen that

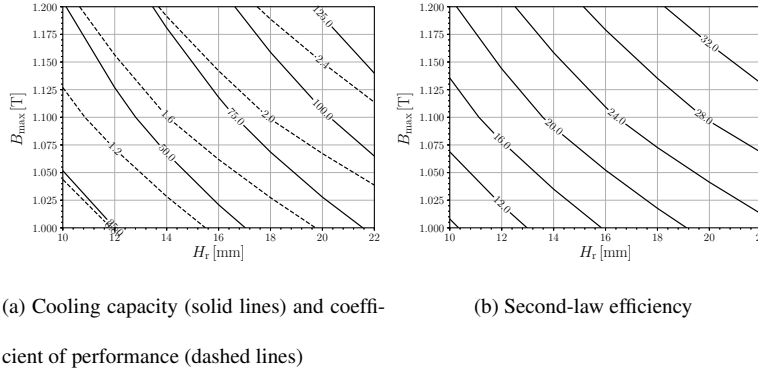


Fig. 17: Performance of the AMR with varying regenerator height and high magnetic field, with fixed $F_M = F_B = 70\%$ and $\Phi = 0.4$

flow profile, and the profile parameters were varied simultaneously with the regenerator geometric parameters. These waveforms can be found in existing MR devices published in the literature. A valve model was also incorporated into a more realistic computation of the coefficient of performance.

When comparing the instantaneous and the rectified cosing magnetic profiles, the cooling capacity associated with the former can be almost 200 % higher than with the latter, for the same utilization and average high magnetic field and considering optimal blow fractions. The rectified cosing profile suffers from high values of the low magnetic field, and reduction of blow fraction up to the minimum tested value of 60 % is not enough to overcome the loss in cooling capacity resulting from this effect.

An analysis of power contributions showed that the cost of the higher cooling capacity for the instantaneous profile is a higher valve power associated with the longer blow duration, dominating the other contributions. However, the coefficient of performance is still higher for the square wave. Hence, even though sinusoidal waveforms can be obtained with

more compact systems, step-like variations of high amplitude of the magnetic field are preferred if performance is more critical.

The ramp magnetic profile is a feasible approximation for the instantaneous profile without abrupt changes in the magnetic field plateaus. For an AMR device operating with this profile and the instantaneous fluid flow profile, both cooling capacity and coefficient of performance are maximized if the blow duration is equal to the period of constant magnetic field; if this exact synchronization is not possible, making the magnetization plateau wider than the flow plateau results in smaller reduction of the performance metrics than if it is narrower.

With this strategy and using average values of utilization, it is possible to achieve second-law efficiency levels compatible with vapor-compression systems. Hence the ramp magnetic profile is identified as a suitable target profile in the design of magnetic circuits for AMR devices.

Supplementary Material

The datasets for the results shown in this paper, the source code used to produce the figures and the \LaTeX manuscript for this work are available at [36].

Conflict of Interest Statement

There is no actual or potential conflict of interest including any financial, personal or other relationships with other people or organizations that could inappropriately influence, or be perceived to influence, the present work.

Acknowledgements This work was funded by the Brazilian Federal Government (CAPES PTI program, Process no. 88887.194773/2018-00, CNPq Grant no. 443696/2014-4 and EMBRAPPII) and by the State of Santa Catarina (FAPESC/INCT). The authors acknowledge the continuous support from Embraco.

References

1. Pradeep Bansal, Edward Vineyard, and Omar Abdelaziz. Status of not-in-kind refrigeration technologies for household space conditioning, water heating and food refrigeration. *International Journal of Sustainable Built Environment*, 1:85–101, 2012.
2. IIR. 36th informatory note on refrigeration technologies: Flammable refrigerants. Available at http://www.iifiir.org/userfiles/file/publications/notes/NoteTech_36_EN_nkyix2fcj7.pdf, 2017. Accessed on October 30th, 2018.
3. S. Lionte, M. Risser, C. Vasile, L. Elouad, and C. Muller. Adapting an active magnetic regenerator to a continuous fluid flow application. *International Journal of Refrigeration*, 85:303–313, 2018. doi: 10.1016/j.ijrefrig.2017.10.009.
4. Anders Smith, Christian R. H. Bahl, Rasmus Bjørk, Kurt Engelbrecht, Karpar K. Nielsen, and Nini Pryds. Materials challenges for high performance magnetocaloric refrigeration devices. *Advanced Energy Materials*, 2:1288–1318, 2012.
5. A. Kitanovski, U. Plaznik, J. Tušek, and A. Poredoš. New thermodynamic cycles for magnetic refrigeration. *International Journal of Refrigeration*, 37:28–35, 2014.
6. Radel Gimaev, Yury Spichkin, Boris Kovalev, Kamil Kamilov, Vladimir Zverev, and Alexander Tishin. Review on magnetic refrigeration devices based on HTSC materials. *International Journal of Refrigeration*, 100:1 – 12, 2019. ISSN 0140-7007. doi: <https://doi.org/10.1016/j.ijrefrig.2019.01.024>. URL <http://www.sciencedirect.com/science/article/pii/S0140700719300404>.
7. A. Greco, C. Aprea, A. Maiorino, and C. Masselli. A review of the state of the art of solid-state caloric cooling processes at room-temperature before 2019. *International Journal of Refrigeration*, 106:66 – 88, 2019. ISSN 0140-7007. doi: <https://doi.org/10.1016/j.ijrefrig.2019.06.034>. URL <http://www.sciencedirect.com/science/article/pii/S014070071930297X>.
8. G. H. Kaneko, A. C. Souza, F. Moro, F. C. Colman, W. A. S. Conceição, C. S. Alves, and P. V. Trevizoli. Design and assembling of a magnetic circuit for a thermomagnetic motor apparatus. *Journal of the*

- Brazilian Society of Mechanical Sciences and Engineering*, 41(10), 2019. ISSN 1806-3691. doi: 10.1007/s40430-019-1898-1. URL <https://doi.org/10.1007/s40430-019-1898-1>.
9. R. Teyber, P. V. Trevizoli, I. Niknia, T. V. Christiaanse, P. Govindappa, and A. Rowe. Experimental performance investigation of an active magnetic regenerator subject to different fluid flow waveforms. *International Journal of Refrigeration*, 74:38–46, 2017.
 10. Alan T. D. Nakashima, Sergio L. Dutra, Paulo V. Trevizoli, and Jader R. Barbosa, Jr. Influence of the flow rate waveform and mass imbalance on the performance of active magnetic regenerators. part I: Experimental analysis. *International Journal of Refrigeration*, 93:236–248, 2018.
 11. F. P. Fortkamp, D. Eriksen, K. Engelbrecht, C. R. H. Bahl, J. A. Lozano, and J. R. Barbosa, Jr. Experimental investigation of different fluid flow profiles in a rotary multi-bed active magnetic regenerator device. *International Journal of Refrigeration*, 91:46–54, 2018. doi: 10.1016/j.ijrefrig.2018.04.019.
 12. Pedro Oliveira Cardoso, Mário Cesar Destro, Manoel Guidi Alvarez, Jaime Andrés Lozano, Jader Riso Barbosa, Jr., and Victor Juliano de Negri. Transient model and energy assessment of a digital solenoid valve system for a magnetic refrigerator. In *Proceedings of the 16th Brazilian Congress of Thermal Sciences and Engineering*, Vitória, 2016.
 13. Pedro Oliveira Cardoso. Um sistema à base de eletroválvulas para o gerenciamento hidráulico de regeneradores magnético-ativos, 2018. Master's Thesis (Mechanical Engineering). In Portuguese.
 14. Alan T. D. Nakashima, Sergio L. Dutra, Gislaine Hoffmann, Jaime A. Lozano, and Jader R. Barbosa, Jr. Performance assessment of solenoid valves as flow distributors for an active magnetic regenerator. In *Proceedings of the 8th International Conference on Caloric Cooling (Thermag VIII)*, Darmstadt, Germany, 2018.
 15. Gislaine Hoffmann, Sergio Luiz Dutra, Pedro Oliveira Cardoso, Alan Tihiro Dias Nakashima, Jaime Andrés Lozano, and Jader Riso Barbosa, Jr. Actuation and control of electric valves for a magnetic refrigerator. In *Proceedings of the 24th ABCM International Congress of Mechanical Engineering (COBEM 2017)*, Curitiba, Brazil, 2017.
 16. R. Bjørk and K. Engelbrecht. The influence of the magnetic field on the performance of an active magnetic regenerator (AMR). *International Journal of Refrigeration*, 34:192–203, 2011. doi: 10.1016/j.ijrefrig.2010.07.004.
 17. Michael A. Benedict, S. A. Sherif, David G. Beers, and Michael G. Schroeder. Design and performance of a novel magnetocaloric heat pump. *Science and Technology for the Built Environment*, 22(5):520–526,

2016. doi: 10.1080/23744731.2016.1185889.
18. Uroš Plaznik, Jaka Tušek, Andrej Kitanovski, and Alojz Poredoš. Numerical and experimental analyses of different magnetic thermodynamic cycles with an active magnetic regenerator. *Applied Thermal Engineering*, 59:52–59, 2013.
19. Paulo V. Trevizoli, Jader R. Barbosa, Jr., Armando Tura, Daniel Arnold, and Andrew Rowe. Modeling of thermomagnetic phenomena in active magnetocaloric regenerators. *Journal of Thermal Science and Engineering Applications*, 6, 2014.
20. Seahn Oh, Seungjae Min, and Jung-Pyo Hong. Air gap flux density waveform design of surface-mounted permanent magnet motor considering magnet shape and magnetization direction. *IEEE Transactions on Magnetics*, 49(5):2393–2396, 2013.
21. Inmyong Park and Sangkwon Jeong. Development of the active magnetic regenerative refrigerator operating between 77 K and 20 K with the conduction cooled high temperature superconducting magnet. *Cryogenics*, 88:106 – 115, 2017. ISSN 0011-2275. doi: <https://doi.org/10.1016/j.cryogenics.2017.09.008>. URL <http://www.sciencedirect.com/science/article/pii/S0011227517301984>.
22. Paulo V. Trevizoli, Theodor V. Christiaanse, Premakumara Govindappa, Iman Niknia, Reed Teyber, Jader R. Barbosa, Jr., and Andrew Rowe. Magnetic heat pumps: An overview of design principles and challenges. *Science and Technology for the Built Environment*, 22(5):507–519, 2016. doi: 10.1080/23744731.2016.1171632.
23. F. P. Fortkamp, J. A. Lozano, and J.R. Barbosa, Jr. Analytical solution of concentric two-pole Halbach cylinders as a preliminary design tool for magnetic refrigeration systems. *Journal of Magnetism and Magnetic Materials*, 444:87 – 97, 2017. doi: 10.1016/j.jmmm.2017.07.072.
24. Fábio P. Fortkamp, Gusttav B. Lang, Jaime A. Lozano, and Jader Barbosa, Jr. Design trade-offs for an active magnetic regenerator device. *Applied Thermal Engineering*, 165:114467, 2020. ISSN 1359-4311. doi: <https://doi.org/10.1016/j.applthermaleng.2019.114467>. URL <http://www.sciencedirect.com/science/article/pii/S1359431119333150>.
25. Paulo V. Trevizoli, Alan T. Nakashima, and Jader R. Barbosa, Jr. Performance evaluation of an active magnetic regenerator for cooling applications – part II: Mathematical modeling and thermal losses. *International Journal of Refrigeration*, 72(206-217), 2016.
26. Donald A. Nield and Adrian Bejan. *Convection in Porous Media*. Springer, New York, 3 edition, 2006.

27. D. Eriksen, K. Engelbrecht, C. R. H. Bahl, R. Bjørk, and K. K. Nielsen. Effects of flow balancing on active magnetic regenerator performance. *Applied Thermal Engineering*, 103:1–8, 2016.
28. K. K. Nielsen, J. Tusek, K. Engelbrecht, S. Schopfer, A. Kitanovski, C. R. H. Bahl, A. Smith, N. Pryds, and A. Poredos. Review on numerical modeling of active magnetic regenerators for room-temperature applications. *International Journal of Refrigeration*, 34:603–616, 2011.
29. C. R. H. Bahl and K. K. Nielsen. The effect of demagnetization on the magnetocaloric properties of gadolinium. *Journal of Applied Physics*, 105, 2009.
30. S. A. Klein. EES — Engineering Equation Solver, Professional Version v9.339. F-Chart Software, 2013. Available at <http://fchart.com>.
31. Tian Lei, Kurt Engelbrecht, Kaspar K. Nielsen, and Christian T. Veje. Study of geometries of active magnetic regenerators for room temperature magnetocaloric refrigeration. *Applied Thermal Engineering*, 111:1232–1243, 2017.
32. I. Niknia, O. Campbell, T. V. Christiaanse, P. Govindappa, R. Teyber, P. V. Trevizoli, and A. Rowe. Impacts of configuration losses on active magnetic regenerator device performance. *Applied Thermal Engineering*, 106:601 – 612, 2016. doi: 10.1016/j.applthermaleng.2016.06.039.
33. G. F. Peixer, J. A. Lozano, and J. R. Barbosa, Jr. Performance evaluation of AMRs using different casings. Book of Abstracts for the Danish Days on Caloric Materials and Devices, 2017.
34. Christian J. L. Hermes and Cláudio Melo. A first-principles simulation model for the start-up and cycling transients of household refrigerators. *International Journal of Refrigeration*, 31(8):1341 – 1357, 2008. doi: 10.1016/j.ijrefrig.2008.04.003,.
35. Cezar O. R. Negrão and Christian J. L. Hermes. Energy and cost savings in household refrigerating appliances: A simulation-based design approach. *Applied Energy*, 88(9):3051 – 3060, 2011. doi: 10.1016/j.apenergy.2011.03.013.
36. Fábio P. Fortkamp, Gustav B. Lang, Jaime A. Lozano, and Jader R. Barbosa, Jr. Polomag/paper-magnetic-profiles v1.0-beta. Available at <https://github.com/Polomag/paper-magnetic-profiles>. Accessed on November 11th, 2019., 2019.